nature communications

Article

https://doi.org/10.1038/s41467-026-69949-1

Gas separation with binary-cooperative heterogeneous membranes

Received: 25 February 2025

Accepted: 11 February 2026

Bo Wang[1] ✉, Chen Zhang[1], Junrui Zhang[1], Ji-kun Yin[1], Xiaomin Song[1], Haochen Ye[1], Qing-hua Li[2], Jun-chao Lao[1] & Tie Wang[1] ✉

Advanced polymer membranes exhibit competitive performance in gas separation. However, rationally designing a polymer membrane with high gas separation performance and structural robustness simultaneously remains challenging. Herein, we present a microzone interfacial polymerization approach to reconstruct the polymer network through the rearrangement of attached functional groups, forming a heterogeneous structure with a crumpled morphology. Unlike common crumpled membranes with homogeneous structures, the heterogeneous structure with a discovered microphase separation endows the membrane with independent and cooperative dual-function regions. The peaks, with more amides as CO_2-philic sites, are functionalized as fast CO_2 transport channels, whereas the stress release effect via the deformation process maintains a high free volume. Valleys, with more rigid phenyls, demonstrate both enhanced CO_2 diffusion and compaction resistance. The cooperative effects of dual-function regions significantly improve the structural robustness, and the optimized membrane exhibits an approximately 300% increase in CO_2 permeance and CO_2/N_2 selectivity compared with its homogeneous counterparts under 1.0 MPa, which is also one order of magnitude greater than that of state-of-the-art membranes. This approach offers a potential pathway for developing more durable polymer membranes suited for harsh environments, which could expand the range of gas separations feasible with membrane technology.

Separation processes, such as evaporation and distillation, which are widely used in gas and liquid separations, are energy-intensive[1]. Membrane separation technology, as an alternative, typically consumes an order of magnitude less energy and has attracted extensive interest[2–7]. Currently, polymer membranes still dominate industrial membranes[8–10]. Various advanced strategies, focused on designing the membrane structure at the molecular level aimed at increasing the gas diffusion or solubility ability or constructing sub-nanometer channels, are conducted to remarkably improve gas permselectivity[11–13]. However, gas separation membranes are mostly applied under operating pressure, and the polymer structure is easily destroyed owing to compaction or plasticization effects, which reduces the separation performance despite the high low-pressure performance.

Strengthening the interchain interactions in the polymer network is a common strategy to suppress the movement of polymer segments[14,15]. Examples of hydrogen bonds[16], metal–ligand bonds[17], and ionic or Coulombic interactions[18] are implemented to effectively dissipate energy and protect the original network stability under external stresses. Other strategies, such as interpenetrating multiple networks, including those with prior mechanical rupture, demonstrate similar effects[19]. However, the introduction of the above interactions inevitably sacrifices the free volume and inhibits the transfer of gas

---

[1]Tianjin Key Laboratory of Life and Health Detection, Life and Health Intelligent Research Institute, Tianjin University of Technology, Tianjin, China. [2]Chemical Engineering Research Center, School of Chemical Engineering and Technology, Tianjin University, Tianjin, China. ✉e-mail: wangbo90@email.tjut.edu.cn; wangtie@email.tjut.edu.cn

molecules, and is capable of forming crystallization areas as stress concentration sites, which tend to form nonselective defects. Bones or teeth in organisms, with alternating arrangements of inorganic phases (hydroxyapatite) and organic phases (collagen), consistently exhibit mechanical robustness. The cooperative effects of the two phases explain the structural stability, which can effectively release external stresses[20–24]. Inspired by this, accurately constructing independent and cooperative functions within polymer networks is an effective approach to improve gas separation performance while maintaining structural stability, especially under operating pressure.

Herein, we designed a heterogeneous polymer membrane through reconstruction of the polymer network, which was achieved using a microzone interfacial polymerization (IP) technique. A microphase separation phenomenon was discovered by detecting the distribution of functional groups, whereas the peaks were composed of more amide groups, and the valleys had more phenyl groups. The resulting cooperative effect endows the membrane with stress release and compaction resistance abilities and enhances CO_2 transport and diffusion abilities. This results in gas separation performance compared with that of state-of-the-art membranes.

Results

Construction and characterization of heterogeneous structures

A heterogeneous structure was constructed through a microzone IP strategy (Supplementary Figs. 1 and 2). In this work, we conducted IP reactions in microzones, i.e., micropores, distributed in a polydimethylsiloxane (PDMS) layer after immersion in an organic phase solution. The swollen micropores (Supplementary Figs. 3c, 4 and 5), formed through solvent-induced swelling mechanism (see Supplementary Fig. 4 for details), are conducive to anchoring organic phase monomers (trimesoyl chloride (TMC)) because of the capillary effect instead of remaining on the surface of the PDMS layer (Supplementary Fig. 15). In Supplementary Fig. 6, the non-uniform concentration gradient of TMC monomers in the swelling PDMS was qualitatively analyzed by Raman depth imaging, where the red areas indicate the regions with a relatively high concentration of TMC monomers. The advantages and purpose of microzone IP reactions are threefold. First, compared with the common liquid–liquid IP process, the construction of microreaction zones is conducive to the uniform distribution of TMC monomers, avoiding the disordered arrangement resulting from interfacial disturbances caused by exothermic reactions. Second, refining the macroscopic liquid–liquid reactions into numerous microreaction units effectively inhibits the reaction rate, making the IP reactions controllable. Third, the IP reactions, which occur at the microporosity, provide more binding sites to enhance the interaction between the selective polymer layer and the PDMS layer. This simple strategy is able to fabricate large-area heterogeneous membranes with a membrane area of 350 cm^2 (Supplementary Fig. 7).

The microphase separation phenomenon in the heterogeneous structure was confirmed by atomic force microscopy-infrared spectroscopy (AFM-IR) (Supplementary Figs. 8 and 9). The heterogeneous structures (Fig. 1a) are observed on the basis of the detection groups of amide groups (C=O, C–N) from Fig. 1d2 to Fig. 1f2 and the phenyl groups (C=C, C–H) from Fig. 1d3–1f3. The PT-4 and PT-5 membranes have homogeneous structures (Fig. 1b, g2–h2, g3–h3). The above results demonstrated that the amide groups mostly accumulated at the peaks rather than at the valleys, whereas the phenyl groups showed the opposite trend. However, this phenomenon cannot be observed using Fourier transform infrared (FTIR) spectroscopy, as shown in Supplementary Fig. 10c. The heterogeneous structure caused by the liquid–liquid (L–L) microzone IP reactions (Fig. 1c, Zone-1) can be obtained within a residence time of 160 s, which was deemed the waiting time after pouring out the TMC solution. In this process, the n-hexane in the micropores carries the TMC monomers to the L-L interfaces (Supplementary Fig. 11, Zone-1), which subsequently promotes the IP reactions, forming a convex structure. The heterogeneous structure, reflected as a crumpled morphology, was characterized by AFM (Fig. 1d1–f1, Supplementary Fig. 12a1–c3) and scanning electron microscopy (SEM, Supplementary Figs. 13a–c and 14a–c). Beyond 160 s (Fig. 1c, Zone-2), a homogeneous structure with a smooth morphology (Fig. 1g1, h1; Supplementary Figs. 12d1–e3, 13d, e and 14d, e), shown as PT-4 and PT-5 membranes, was achieved from the liquid–solid (L–S) microzone IP reactions (Supplementary Fig. 11, Zone-2), caused by the confined movement of TMC monomers to contact piperazine (PIP) monomers. The membranes fabricated with PIP concentrations of 0.2 and 0.3 wt% are shown in Supplementary Fig. 19 and exhibit the same variation tendency as membranes fabricated with a PIP concentration of 0.1 wt%.

The microphase separation phenomenon is attributed to the change in crosslinking density from the PT-1 to the PT-5 membranes, which was analyzed using X-ray photoelectron spectroscopy (XPS). As shown in Supplementary Table 1, the degree of crosslinking of heterogeneous membranes (PT-1 to PT-3) is significantly greater than that of homogeneous membranes (PT-4 and PT-5), indicating the formation of dense structures. Moreover, the increase in the O/N ratio from the PT-1 to PT-3 membranes indicates an increase in linear crosslinking structures in the resultant PA membranes. This suggests that the acyl chloride groups on the PDMS surface were partially hydrolyzed to form carboxyl groups when in contact with the PIP solution, reducing the crosslinking density. Hence, the composition differences at the peaks and valleys stem from the variations initiated at the micropores and surface on the PDMS layer in the IP processes, which subsequently changed the crosslinking density.

Formation mechanism of heterogeneous structure

The formation mechanism of the heterogeneous structure, explained as the L–L microzone IP reaction, was illustrated by Raman scanning spectroscopy. We detected different functional groups by adjusting the Raman focusing mode to observe the microphase separation phenomenon. In the autofocus mode, the Raman laser focuses on the highest location of the membrane surface, which is the peak in the crumpled morphology. Discrete red points, representing C=O or C–N groups in the nascent polyamide films (Fig. 2a1), appear at the initial contact of PIP and TMC monomers (Fig. 2a1-1). This produces large polyamide films through continuous IP reactions (Fig. 2a2), as reflected by the dense red points in Fig. 2a2-1. In Fig. 2a3-1, adjacent large polyamide films are capable of decreasing the surface energy, followed by incorporation with other adjacent polyamide films to obtain the final crumpled morphology (Fig. 2a3). In fixed focus mode, the Raman laser is limited to the mPSf surface, which is regarded as the valley in the crumpled morphology. Unlike the results in Fig. 2a1-1–a3-1, dense red points, representing the C=C or C–H groups in Fig. 2a4-1, appear immediately on the mPSf surface, followed by a decrease in density with continuous reaction in Fig. 2a5-1, which indicates the growth of nascent polyamide films (Fig. 2a5). The disappearance of the red points indicates the cavity structure of growing polyamide films. The significant decrease in the red point density in Fig. 2a6-1 reflects the incorporation of polyamide films, which results in peaks with a crumpled morphology corresponding with the results in Fig. 2a3-1. The formation mechanism of the homogeneous structure, as reflected by the smooth morphology, is explained by the L-S IP reaction shown in Fig. 2b. As shown in Fig. 2b1–b3, the absence of solvents in the micropores makes it difficult to induce TMC to contact PIP consecutively to participate in the IP reaction; therefore, the formed polyamide films are difficult to grow or incorporate further. The final smooth morphology is obtained through the compact packing of polyamide films, which shows the gradual densification of red points in the Raman signals from Fig. 2b1-1–b3-1. Here, the result is independent of the selected functional groups.

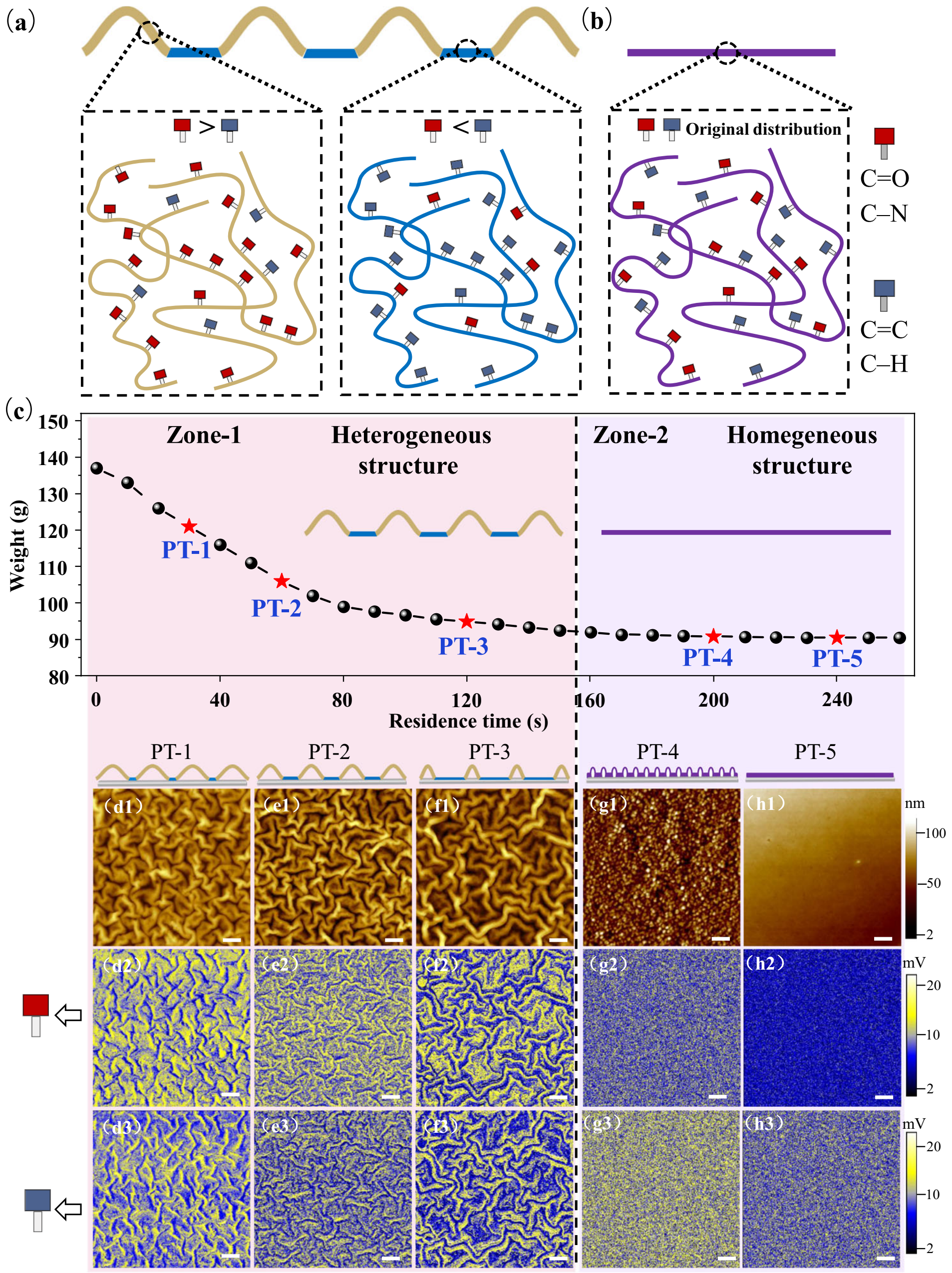

Fig. 1 | Construction of heterogeneous and homogeneous structures using the microzone IP reaction and AFM surface images of the PT-1 to PT-5 membranes. Diagram of the (**a**) heterogeneous structure and (**b**) homogeneous structure of the polyamide membranes. The yellow and blue symbols represent peaks and valleys in the crumpled polyamide membranes with heterogeneous structure, while the purple ones represent the flat polyamide membranes with homogeneous structure. The red and gray rectangles mean C=O and C–N groups, and C = C and C–H groups, respectively. **c** The change in weight with the residence time of the swollen PDMS layer. AFM surface images from (**d1**) to (**h1**) and corresponding AFM-IR phase diagrams from (**d2**) to (**h3**). **d2**–**h2** Images were obtained by detecting C=O and C–N groups, whereas (**d3**–**h3**) images were obtained by detecting C=C and C–H groups. Scale bar: 200 nm.

Mechanical properties of heterogeneous membranes

The cooperative effects of deformation and compaction resistance explain the mechanical properties of heterogeneous membranes, which can effectively alleviate both horizontal and vertical stresses. Tensile tests were performed to simulate the horizontal stresses on the membrane (Supplementary Fig. 20). The sample was stretched to a fixed value, held for 15 s, and then recovered. This process was repeated twice. As shown in Fig. 3b, the average tension force from the PT-1 to PT-5 membranes gradually increased from 840 ± 20 to 2650 ± 20 mN. Specifically, the tension force of the PT-1, PT-2, and PT-3 membranes gradually decreases with increasing holding time, and parts of the crumpled morphology became smooth under a stretched state (Supplementary Fig. 21), indicating that the crumpled morphology is capable of releasing stress. Within one hundred cycles of stretch tests (Fig. 3a1–a6, Supplementary Fig. 22), no visible cracks or fragmentation of the PT-1 to PT-3 membranes were observed, whereas the PT-4 and PT-5 membranes exhibited obvious cracks after five cycles (Fig. 3a7–a10). These results reflect the deformation characteristics of the crumpled morphology, thus effectively avoiding membrane defects, which is also confirmed by the tensile tests shown in Supplementary Fig. 23. Gold nanoparticle retention tests were also conducted to visually analyse the deformation behavior of the peaks, and the detailed process is shown in the Supplementary Information. As shown in Fig. 3e and Supplementary Fig. 16, gold nanoparticles were used as

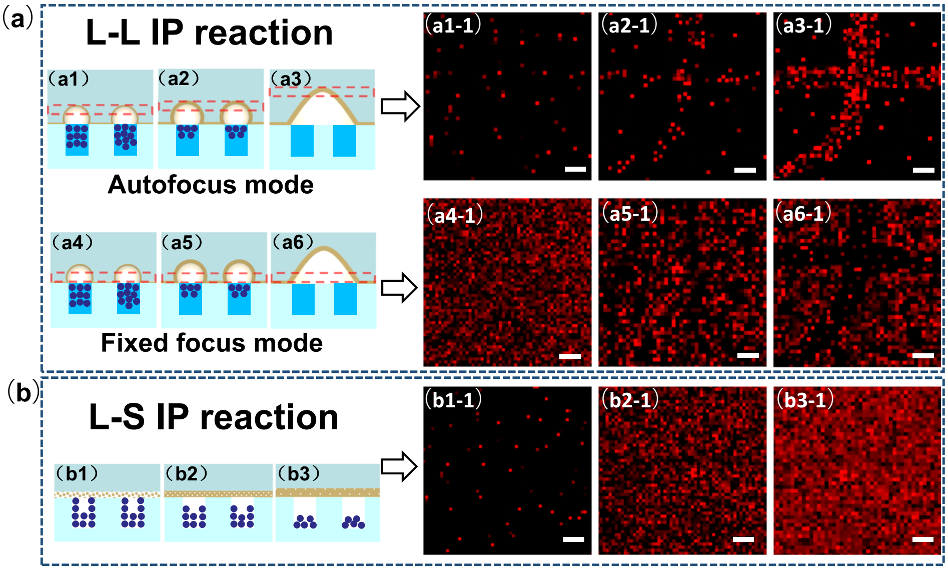

Fig. 2 | Formation mechanism of the heterogeneous and homogeneous structures. a Schematic of the heterogeneous structure (PT-1, PT-2, and PT-3) formation process with the L-L IP reaction from (a1) to (a6) and corresponding Raman scanning analysis from (a1-1) to (a6-1). The yellow symbols represent the nascent polyamide films. The red rectangular dotted lines indicate the Raman focusing in autofocus mode (a1–a3) and a fixed focus mode (a4–a6), respectively. Here, (a1)–(a3) and (a4)–(a6) represent the formation and growth of nascent polyamide films and the formation of peaks and valleys in a crumpled morphology, respectively. **b** Schematic of the homogeneous structure (PT-4 and PT-5) formation process by the L-S IP reaction from (b1) to (b3) and corresponding Raman scanning analyses from (b1-1) to (b3-1). The purple points and blue rectangles indicate the TMC monomers and n-heptane in the micropores of the swollen PDMS layer. Scale bar: 100 nm.

the markers, accompanied by a high-speed gas flow to strike the membrane. The deformation effect of the peaks effectively releases compressive stress (Fig. 3f), which is verified by narrowing the peak width from d1 to d2 to d3 (Fig. 3f1–f3, f1-1–f3-1) from atmospheric pressure to high pressure.

AFM height images and their corresponding quantitative nanomechanical maps were used to simulate the vertical stresses on the membrane surface. Original SEM cross-section images are shown in Fig. 3c and Supplementary Figs 17 and 18. Four parameters are shown in Fig. 3d: the indentation depth, which reflects the deformation space when the membrane is closely attached to the substrate (mPSf membrane); the crumpled distance, which reflects the crumpled density; the crumpled height, which indicates the fluctuation degree of the crumpled structure; and the Young's modulus, which reflects the difficulty in deformation. As shown in Supplementary Fig. 44e, the average crumpled heights from the PT-1 to PT-5 membranes gradually decreased from 128.2 ± 3.2 to 95.1 ± 2.3 nm and then rapidly decreased to 3.3 ± 0.2 nm. This finding suggests the disappearance of the crumpled morphology. The increase in the crumpled distance increases from 12.1 ± 1.3 to 125.1 ± 3.3 nm, which demonstrates a decrease in the crumpled density. AFM mechanical phase diagrams verify the mechanical microphase separation (Fig. 3g), demonstrating that the Young's modulus at the peaks (yellow domains) is lower than that at the valleys (purple domains). We further used the AFM mechanical mode to compare the peaks and valleys in detail. In Fig. 3h, the Young's moduli at the peaks from the PT-1 to PT-3 membranes are lower than those at the valleys, reflecting a greater indentation depth at the peaks than at the valleys. The indentation depth changes with attached force on the AFM tip, but the calculated Young's modulus is almost independent of attached force (Supplementary Fig. 44a–c). However, the PT-4 and PT-5 membranes, which have relatively low Young's moduli, are compressible. Specifically, the indentation depth at valleys is lower than that in homogeneous membranes (PT-4 and PT-5). This result shows the enhanced compression resistance because of microphase separation, which increases the distribution of rigid groups at the valleys.

Gas separation performance of heterogeneous membranes

The heterogeneous membrane demonstrated gas separation performance under operating pressure. In Fig. 4a, at a pressure of 1.0 MPa, the CO_2 permeance increases from 2350 GPU to 2967 GPU from the PT-1 to PT-3 membranes and then rapidly decreases to 706 GPU (PT-5 membrane). However, the CO_2/N_2 selectivity decreases slowly and then rapidly from the PT-1 to the PT-3 to the PT-5 membranes. The PT-3 membrane exhibited the highest CO_2 permeance and acceptable CO_2/N_2 selectivity. The gas separation performance of the mPSf membrane is almost independent of pressure, indicating that pressure has no effect on the performance of PT membranes (Supplementary Fig. 26). The CO_2/N_2 separation performance with pressure is shown in Supplementary Figs. 27 and 28, and the CO_2 and N_2 permeance tested with pure gas is shown in Supplementary Fig. 35. Both the CO_2 permeance and CO_2/N_2 selectivity of the PT-1, PT-2 and PT-3 membranes decrease slightly at low pressure and remain constant at operation pressure, but those of the PT-4 and PT-5 membranes decrease rapidly. According to the pressure cycle measurements in Supplementary Fig. 29, the heterogeneous membrane shows the same performance during increased and decreased pressures. On the basis of the pressure stability tests in Supplementary Fig. 30, the membrane performance is unchanged under the same pressure within a certain time. The PT-3 membrane treated at 120 °C for 4 h to simulate the real temperature of the flue gases in Supplementary Fig. 31 shows the same performance as that at room temperature, whereas the performance of the PT-5 membrane greatly decreases. The stretch tests also revealed the performance stability of heterogeneous membranes at different tensile rates (Fig. 4b and Supplementary Fig. 32). Figure 4c and Supplementary Table 4 compare the heterogeneous membranes in this study with other state-of-the-art membranes under 1.0 MPa reported in the literature that demonstrate great advantages in terms of gas separation performance. Moreover, the PT-1, PT-2 and PT-3 membranes also exhibited CO_2/CH_4 and CH_4/N_2 separation abilities within 3.0 MPa (Supplementary Fig. 33). The CH_4/N_2 separation ability is attributed to a high CH_4/N_2 solubility selectivity, which was obtained through deconvoluting the CH_4 and N_2 permeability into solubility and diffusivity coefficients on

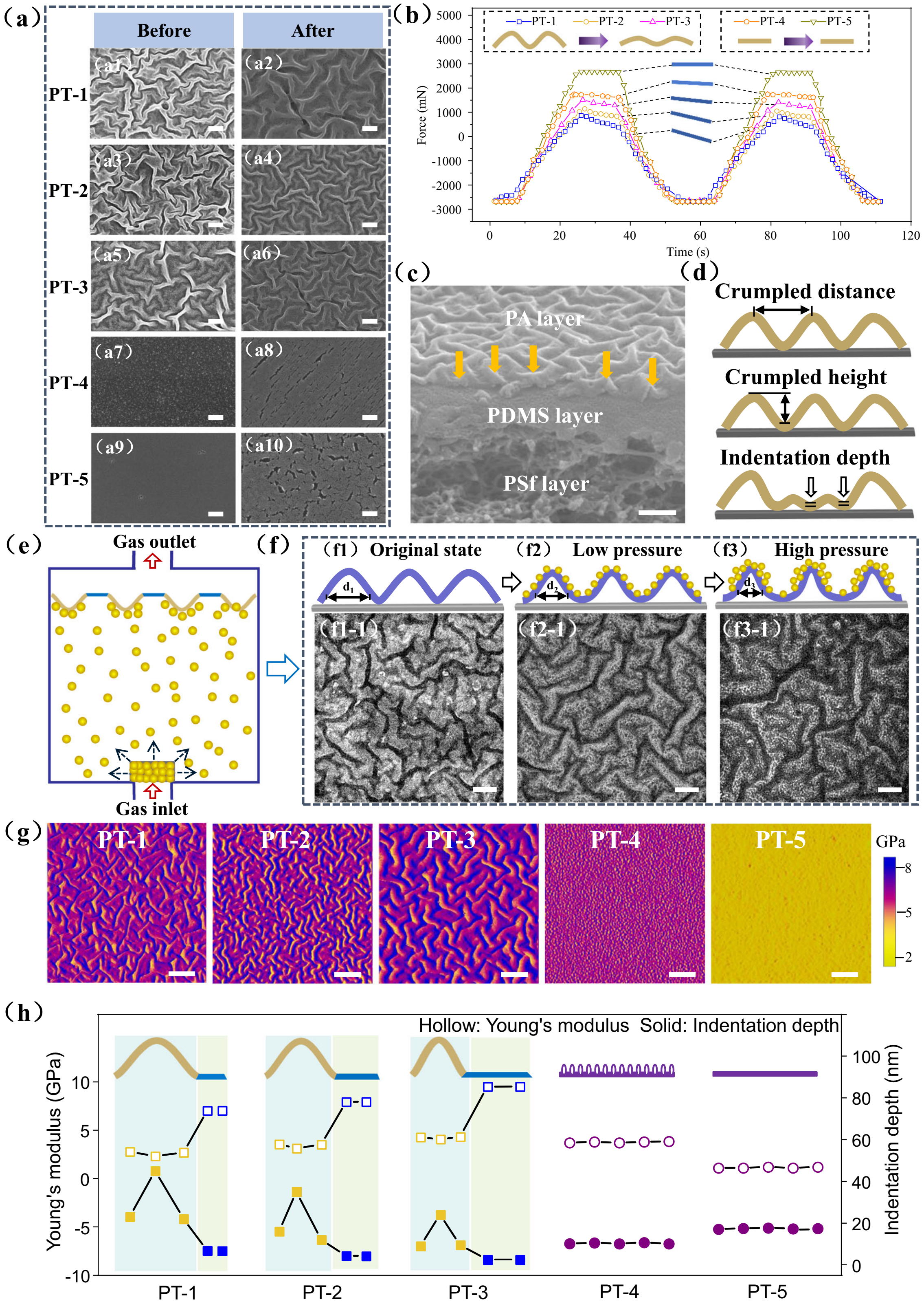

the basis of the solution–diffusion model (Supplementary Fig. 34, Tables 2 and 3). Meanwhile, within operation pressure (from 1.0 to 3.0 MPa), the crumpled structure still cannot be squeezed onto the mPSf membrane (Supplementary Fig. 44d).

The rearrangement of functional groups at the peaks and valleys endows the crumpled membrane with independent and cooperative dual-function regions. These regions can improve the membrane performance through increased gas diffusion and increased pressure resistance. Gold nanoparticle retention tests (Supplementary Fig. 36) were conducted to provide visual evidence of the diffusion difference in the heterogeneous structure (Supplementary Figs. 37–39). We fabricated a homogeneous crumpled membrane (Supplementary Fig. 8f–f3) with a common L-L IP reaction to compare the gas transfer behavior with that of a heterogeneous crumpled membrane at

Fig. 3 | Mechanical properties of the heterogeneous and homogeneous membranes. a SEM images of the PT-1 to PT-3 membranes (a1), (a3), (a5) before and (a2), (a4), (a6) after one hundred cycles of stretching and the PT-5 membrane (a7), (a9) before and (a8), (a10) after five cycles of stretching. Scale bar: 200 nm. The yellow symbols indicate the polyamide membranes with crumpled or flat morphology. **b** Recycled tension test on PT-1 to PT-5 membranes at a stretch rate of 5% in an AES-4SD flexible electronic device comprehensive test platform. **c** The cross-section image of the PT-3 membrane. The yellow arrows indicate the cavity structure at peaks. Scale bar: 200 nm. **d** Schematics of the crumpled distance, crumpled height, and indentation depth were tested using the AFM force model. **e** Deposition process of gold nanoparticles (yellow spheres) on PT-1 membrane with **f** different pressure states: (f1) Original state, (f2) low operation pressure (1.0 MPa) and (f3) high operation pressure (3.0 MPa), and the corresponding TEM images are shown in (f1-1), (f2-1), and (f3-1). Scale bar: 200 nm. The purple symbols reflect the change of the crumpled structure under different pressures. **g** AFM mechanical phase diagrams of the PT-1 to PT-5 membranes. Scale bar: 1 μm. **h** Young's modulus and indentation depth of the PT-1 to PT-5 membranes. For the PT-1, PT-2, and PT-3 membranes, the indentation depths at the peaks were calculated by subtracting the corresponding crumpled heights in Supplementary Fig. 43e. Three data points were collected at the peaks, and two data points were collected from the valleys.

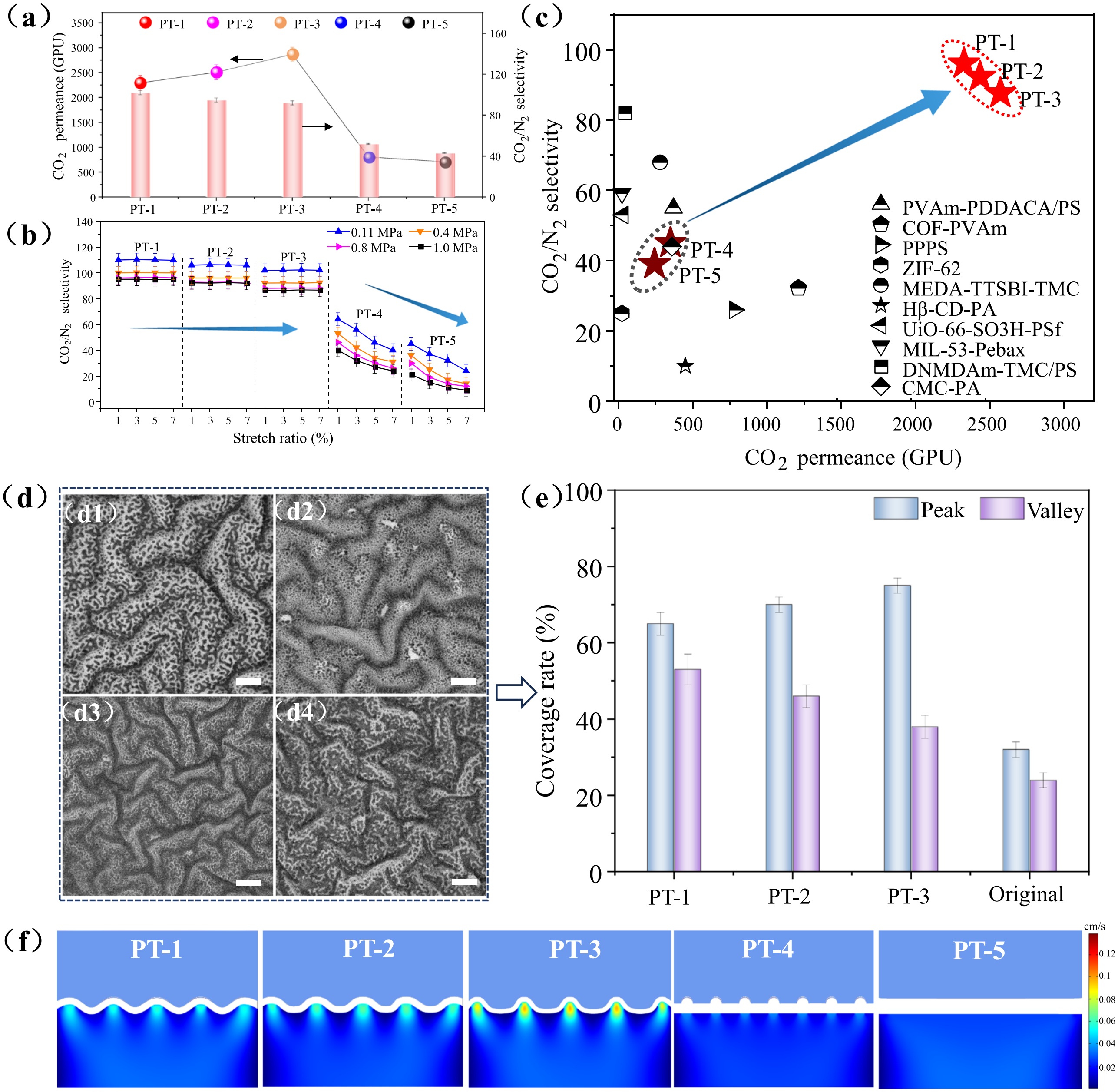

Fig. 4 | Gas separation performance, comparison with other membranes, and gas transport mechanism from the PT-1 to PT-5 membranes. a The CO_2 permeance and CO_2/N_2 selectivity of the PT-1, PT-2, PT-3, PT-4, and PT-5 membranes. Test pressure: 1.0 MPa. **b** CO_2/N_2 selectivity of the PT-1, PT-2, PT-3, PT-4, and PT-5 membranes with different stretch rates. Test pressure: 1.0 MPa. **c** CO_2 permeance and CO_2/N_2 selectivity of the PT-1 to PT-5 membranes at 1.0 MPa compared with those of other reported membranes. The five-pointed stars represent the membrane fabricated in this work. **d** TEM images of PT-1, PT-2, PT-3, and original homogeneous crumpled membranes deposited with gold nanoparticles. Scale bar: 200 nm. **e** Coverage rates of gold nanoparticles on the peaks and valleys of PT-1, PT-2, PT-3 and the original homogeneous crumpled membranes. Test time: 30 min. **f** Simulation results of the variation in the velocity field from the PT-1 to PT-5 membranes on the permeation side. The error bars in (**a**, **b**, **e**) represent mean ± SD ($n = 3$).

1.0 MPa, and the results are shown in Fig. 4d, e. In this process, gases can pass through the membrane, whereas the gold nanoparticles remain on the surface. Moreover, the gold nanoparticles, which have the same charge as the PT membranes in Supplementary Table 5, cannot be adsorbed on the membrane surface. Hence, the retention of gold nanoparticles was used to judge the gas transfer rate. In Fig. 4e, the coverages of the gold nanoparticles at both the peaks and valleys of the heterogeneous membranes are greater than those of the homogeneous membranes within a fixed time, which demonstrates that the heterogeneous structure is critical for improving gas transfer. In this structure, more amide groups accumulate at the peaks, remarkably increasing the CO_2 solubility and constructing rapid gas transfer channels, whereas the phenyl groups in valleys maintain a high free volume due to steric hindrance effects. This is beneficial for improving the gas diffusion ability, especially under operating pressure. The largest coverage rate of gold nanoparticles in the PT-3 membrane explains the highest CO_2 permeance shown in Fig. 4a. The rapid decrease in the CO_2/N_2 selectivity of the PT-4 and PT-5 membranes is mainly attributed to the facilitated transport mechanism[25–27].

Two-dimensional resistance models[28] and COMSOL Multiphysics simulations were introduced to better understand the gas transport behavior in heterogeneous structures. In the resistance model shown in the Supplementary Information, the relationship describing gas permeation through a polymer membrane via Fick's law is mathematically equivalent to Ohm's law, which describes current flow through a resistor. Hence, the gas permeation rate is inversely proportional to the gas transport resistance. In Supplementary Fig. 40, the resistances of the heterogeneous crumpled membrane (R_1), homogeneous crumpled membrane (R_2), and homogeneous smooth membrane (R_3) were calculated as $R_i = 1/BA_i$ (R, B, and A represent the gas transport resistance, gas permeance, and surface area, respectively), and the results are shown in Supplementary Table 6. The results show that with increasing operation pressure, the gas transport resistance of the homogeneous structure increases rapidly, whereas that of the heterogeneous structure increases slowly. The series resistance model[29] was also introduced to analyze the heterogeneous crumpled structure compared with the counterparts. From Supplementary Fig. 41 and Table 7, the result shows that the CO_2 permeance of the selective layer is obviously higher than that of the corresponding composite membranes, which indicates the total resistance of the composite membrane is mainly decided by the selective layer. Meanwhile, the CO_2 permeance of heterogeneous polyamide layers is remarkably higher than that of the homogeneous counterparts, indicating the heterogeneous structure endows polyamide with enhanced gas permeation ability. Moreover, the mPSf membrane, which has a low resistance compared with other membranes with PA layers, has almost no effect on the overall resistance. We also conducted numerical simulations of the gas diffusion rate on the membrane permeate side using COMSOL Multiphysics to analyze this process, and the calculation method is described in the Supplementary Information and Supplementary Fig. 42. In Fig. 4f, the gas diffusion rate through the peaks is significantly higher than that through the valleys. Similar to the results in Fig. 4e, the PT-3 membrane also has the highest gas diffusion rate, which is also attributed to the low crosslinking density compared with those of the PT-1 and PT-2 membranes (Supplementary Table 1). Furthermore, the heterogeneous structure can effectively avoid the production of stress concentration points between peaks and valleys (Supplementary Fig. 43), which is vital for decreasing the number of membrane defects, especially under consecutive stress effects.

To analyse the economic advantages of heterogeneous membranes for CO_2 capture, a typical two-stage membrane process was simulated on the basis of the assumptions of our previous study[30]. The detailed calculation process and a comparison of all the membranes are shown in Supplementary Fig. 45 and Table 8. The CO_2 capture energy consumption (Supplementary Fig. 45a) decreases with pressure and then increases, as explained in our previous report[31]. As shown in Supplementary Fig. 45b, the membrane area requirements decrease with pressure due to the increased driving force. Overall, the CO_2 capture cost decreases with pressure (Supplementary Fig. 45c). The PT-3 membrane has a minimum CO_2 capture cost of \$26.2 per tonne of CO_2 at 0.8 MPa, which shows good potential for CO_2 capture.

Discussion

Common polymer membranes always suffer from a trade-off effect between gas separation ability and structural stability, which restricts their application under harsh conditions. In this work, we successfully constructed a heterogeneous membrane with microzone IP technology. The discovered microphase separation endows the membrane with independent and cooperative dual-function regions through the rearrangement of functional groups at peaks and valleys, which explains the rapid gas transfer of the membrane while maintaining structural stability. The heterogeneous membranes exhibit optimal CO_2/N_2 separation ability under pressure, where they are both more permeable and selective than their homogeneous counterparts and are reported to be state-of-the-art membranes. This design strategy can be extended to produce other heterogeneous membranes with various cooperative effects, such as attraction and repulsion, order and disorder, as well as polarity and nonpolarity, achieved by changing the reaction substances or fabrication conditions. These changes can be expected to achieve the efficient separation of difficult-to-separate systems, e.g., isomers. In addition to the separation performance, the cooperative effects can also improve other properties of the membrane, such as its mechanical properties, which can effectively protect the membrane structure under harsh environments and further broaden its application fields, such as high-temperature and acidic or alkaline conditions.

Methods

Preparation of the mPSf membrane

Polydimethylsiloxane (PDMS, 0.25 g, 0.5 wt.%), dibutyltin dilaurate (DBD, 0.2 g, 0.4%), and tetraethyl orthosilicate (TEOS, 0.2 g, 0.4 wt.%) were dissolved in n-heptane and stirred at 35 °C for 30 min under humidified conditions, thus obtaining PDMS prepolymer solution. PDMS, DBD, and TEOS were used as monomers, catalysts, and crosslinking agents, respectively, in the crosslinking reaction. The PSf ultrafiltration support was immersed in sodium dodecyl sulfate (SDS, 0.5 wt%) solution to remove organic solvent retained in the membrane pores, followed by drying at 60 °C for 10 h. The treated PSf membrane was coated with a PDMS solution, with a preset wet coating thickness (the gap between the PSf support and coating knife) of 200 μm (gap accuracy ± 5 μm), whereas the thickness of the PDMS layer in the mPSf membrane was approximately 100 nm. The casting membranes were dried at 30 °C and 40% RH in an artificial climate chamber (Climacell 222R, Germany) for at least 2 h. The treated PSf support was denoted as the modified PSf (mPSf) membrane.

Fabrication of heterogeneous crumpled membranes

The membrane was fabricated using a microzone IP process. The aqueous phase solution was fabricated with 0.1–0.3 wt% PIP and 0.1 wt % Na_2CO_3, and 0.1 wt% TMC dissolved in hexane was used as the organic phase solution. The amide groups formed using the IP reaction constitute the repeating units in the polymer segments of the crumpled membrane. The prepared solutions were sealed and stored in a water bath at 25 °C for 30 min to avoid solvent evaporation. First, the mPSf membrane, which was clamped between two Teflon frames, was immersed in 30 mL of TMC solution for 3 min. Then, the excess solution was removed. Then, the membrane was incubated for 30 s, 60 s, 120 s, 200 s, and 240 s as the residence time. Then, the treated mPSf membrane was immediately soaked in 50 mL of PIP solution for 15 min. Subsequently, the resulting membrane was washed thoroughly with deionized water and dried at 30 °C and 40% RH for 12 h. The obtained heterogeneous membrane with a crumpled morphology was attached to the mPSf membrane, forming a selective layer of the membrane. The membranes fabricated with different residence times of 30 s, 60 s, 120 s, 200 s, and 240 s were named the PT-1, PT-2, PT-3, PT-4, and PT-5 membranes, respectively. Among them, the PT-1, PT-2, and PT-3 membranes have heterogeneous structures with crumpled morphologies, whereas the PT-4 and PT-5 membranes are homogeneous with smooth morphologies.

Fabrication of homogeneous crumpled membranes

The membrane was fabricated via a common liquid–liquid IP process. The aqueous phase solution was fabricated with 0.1 wt% PIP and 0.1 wt % Na_2CO_3 (A solution), and 0.1 wt% TMC dissolved in hexane (B solution) was used as the organic phase solution. The prepared solutions were sealed and stored in a water bath at 25 °C for 30 min to avoid solvent evaporation. First, 50 mL of A solution was poured into the beaker, and then 50 mL of B solution was slowly added and left for 15 min. A polyamide film was formed at the interface of the two phases, after which it was extracted with a substrate. The obtained homogeneous crumpled membrane, attached to a mPSf membrane, was used to compare the mixed-gas separation performance with its heterogeneous counterpart. The resultant homogeneous crumpled membrane, attached to a PSf support, was used to compare the pure-gas selectivity with its heterogeneous counterpart to judge the gas transfer mechanism. The resulting membrane was washed thoroughly with deionized water and dried at 30 °C and 40% RH for 12 h.

Characterizations of the membranes

The morphology of the membranes was characterized using SEM (nano-SEM 430, FEI, USA) and AFM (Bruker, Dimension IconXR, Germany). AFM was also used to characterize the membrane surface morphology and obtain information, including indentation, crumpled height, and crumpled distance. AFM-IR (Bruker, Anasys nanoIR3s, Germany) nanoinfrared spectroscopy was used to perform microzone chemical analysis to characterize the microphase separation of the functional groups. FTIR spectroscopy of the membranes in the wavenumber range of 400 to 4000 cm^{-1} was performed using an FTS-6000 instrument (Bio-Rad, USA). XPS (ESCALAB 250Xi, Thermo Fischer, USA) was used to characterize the element composition and degree of crosslinking of the crumpled membrane with Al Kα radiation. X-ray diffraction (XRD) analysis ($2\theta = 10°$ to $50°$) was performed at room temperature with a Bruker-AXS D8 diffractometer with a Cu Kα ($\lambda = 1.54$ Å) radiation detector. Raman spectroscopy (Renishaw, inVia Qontor, Britain) was used to analyse the TMC distribution in the swollen PDMS layer and the C=O, C=C, C−H, and C−N groups in the membrane. A Raman scanning model, which is based on different functional groups, was used to demonstrate the formation process of peaks and valleys in the crumpled structure. Gold nanoparticle retention tests were conducted to provide visual evidence of the difference in gas diffusion between the peaks and valleys of the heterogeneous structure, and the detailed testing process is described in the Supplementary Information. N_2 adsorption-desorption isotherms of the swelling PDMS layer were performed on BSD-660M (Beishide Instrument, China) at 77 K, and the pore size distribution of the PDMS layer was calculated based on the Barrett-Joyner-Halenda (BJH) model. The swelling PDMS layer was peeled off the mPSf membrane by immersing into N, N-dimethylformamide (DMF) to eliminate the influence of the PSf substrate on the analysis of pore size. Subsequently, the PDMS layer was rinsed with ethanol and vacuum degassed at 25 °C for 10 h to remove the residual solvent before testing.

Mechanical property measurement

The membrane was cut into a square of 1 cm × 1 cm, and the effect of vertical force was tested by AFM (Bruker, Dimension IconXR, Germany). The effect of horizontal stretch tension was tested using a mechanical test module in an AES-4SD flexible electronic device comprehensive test platform with different stretch rates. The mechanical properties, including the Young's modulus, were gauged using peak force quantitative nanomechanical mapping (PF-QNM) imaging via AFM. The RTESPA-525-30 was used as the AFM tip to conduct the PF-QNM experiment, which is composed of 0.01-0.025 Ωcm Antimony (n)-doped Si with an aluminum reflective coating on the backside of the cantilever. The tip and cantilever parameters are presented below. The tip parameters included a tip height of 10−15 μm and an end curvature radius of 30 nm; the cantilever parameters included a cantilever thickness of 5.75 μm, a cantilever length of 125 μm, a cantilever width of 40 μm, a cantilever frequency of 525 kHz, and a spring constant of 200 N/m. The selected tip with a large spring constant of 200 N/m has a hardness property that is beneficial for rapid scanning. Moreover, the cantilever is difficult to deform and can truly reflect the indentation depth. A selected tip with a high resonance frequency of 525 kHz quickly reaches the equilibrium state. Thus, for the crumpled structure with a large undulation, the morphology can be rapidly detected. This is consistent with the SEM results, indicating that the crumpled structure is close to the PSf support. A selected tip with a curvature radius of 30 nm can avoid damage to the ultrathin sample surface caused by the contact between the tip side and the sample. In this work, the applied force on the membrane surface via AFM tips converted to the gas pressure is large enough to squeeze the peaks tightly on the mPSf surface, and the testing process was shown in Supplementary Fig. 44. Hence, the tested Young's modulus of the peak, similar to the valley, was also obtained via pressing the peaks tightly on the mPSf support, which can eliminate the influence of morphology on the test results. Before and after performing each test, the deflection sensitivity calibration was performed on a sapphire sample that was assumed to have a less than 5% error. Meanwhile, the tip radius was calibrated using a standard highly oriented pyrolytic graphite film (18 GPa). This calibrated tip radius (35 ± 3 nm), which accounts for tip blunting, was used for all subsequent contact area calculations and modulus extractions from our samples.

Gas permselectivity test

The gas permselectivity of the membranes was tested with custom-made testing equipment[27]. The feed gas passed through a humidifier at 35 °C and a dehumidifier at ambient temperature successively so that the feed gas was saturated with water vapor before it entered the test unit. Thus, in this study, the humidified conditions were 100% relative humidity. The structure of the membrane cell is shown in Supplementary Fig. 24. The detailed gas permeance (R) is expressed in units of GPU, and the $CO_2/N_2(CH_4)$ selectivity equals the CO_2 permeance divided by the $N_2(CH_4)$ permeance.

The permeance is calculated via Eq. (1) as follows:

$$R = \frac{Q_i}{A \cdot \Delta P_i} \qquad (1)$$

where Q_i represents the permeate flow rate through the membrane, A is the effective membrane area, and ΔP_i is the partial pressure difference between the upstream and downstream sides of the membrane. A was calculated using the following two methods because of the crumpled morphology with different membrane surfaces. One is the real area obtained from the AFM results in Supplementary Fig. 25, and the other is the fixed area of the membrane cell. In the main text, all the performances were calculated with real areas.

The single-gas permeabilities P (Barrer) of the crumpled membranes were evaluated using a Labthink VAC-V2(EX) apparatus based on the constant volume/variable-pressure method. In this work, we utilized the stacked PA layers, with a thickness of about 50 μm, to perform the time-lag measurements, which can effectively eliminate the impact of porous support. The PA layer was delaminated from the composite membrane by immersing it in n-hexane to remove the mPSf support, which will not damage the PA layer. The peeled PA layer with a surface area of 30 cm^2 should be carefully transferred with a glass plate, and then this process was repeated to accumulate more PA layers. The stacked PA layers were treated at 120 °C in a vacuum and then compressed at 3.0 MPa before testing to remove the residual solvent. To reduce the workload, after collecting some PA layers, we folded them several times to increase the effective thickness. The measurement was carried out on circular membrane samples fabricated by masking with adhesive aluminum foil with an effective exposed area of 3.14 cm^2. The diffusivity coefficient D ($cm^2\ s^{-1}$) was calculated using the time lag method as expressed in Eq. (2):

$$D = \frac{l^2}{6\theta} \tag{2}$$

where l is the membrane thickness and θ is the time lag of the permeability measurement.

The solubility coefficient S (cm^3 (STP) $cm^{-3}\ cmHg^{-1}$) was calculated from the ratio of the gas permeability coefficient to the diffusivity coefficient using Eq. (3) as follows:

$$S = \frac{P}{D} \tag{3}$$

Data availability

All data are available from the corresponding author upon request. The data generated in this study are provided in the Source data file. Source data are provided with this paper.

References

1. Sholl, D. S. & Lively, R. P. Seven chemical separations to change the world. *Nature* **532**, 435–437 (2016).
2. Bernardo, P., Drioli, E. & Golemme, G. Membrane gas separation: a review/state of the art. *Ind. Eng. Chem. Res.* **48**, 4638–4663 (2009).
3. Hennessy, J. Membranes from academia to industry. *Nat. Mater.* **16**, 280–282 (2017).
4. Luo, X. et al. Wrinkled metal-organic framework thin films with tunable Turing patterns for pliable integration. *Science* **385**, 647–651 (2024).
5. Shi, X. et al. Selective liquid-phase molecular sieving via thin metal–organic framework membranes with topological defects. *Nat. Chem. Eng.* **1**, 483–493 (2024).
6. Zhou, S. et al. Asymmetric pore windows in MOF membranes for natural gas valorization. *Nature* **606**, 706–712 (2022).
7. Datta, S. J. et al. Rational design of mixed-matrix metal-organic framework membranes for molecular separations. *Science* **376**, 1080–1087 (2022).
8. Karan, S., Jiang, Z. W. & Livingston, A. G. Sub-10 nm polyamide nanofilms with ultrafast solvent transport for molecular separation. *Science* **348**, 1347–1351 (2015).
9. Jimenez-Solomon, M. F. et al. Polymer nanofilms with enhanced microporosity by interfacial polymerization. *Nat. Mater.* **15**, 760 (2016).
10. Galizia, M. et al. 50th Anniversary Perspective: polymers and mixed matrix membranes for gas and vapor separation: a review and prospective opportunities. *Macromolecules* **50**, 7809–7843 (2017).
11. Sandru, M. et al. An integrated materials approach to ultrapermeable and ultraselective CO_2 polymer membranes. *Science* **376**, 90–94 (2022).
12. Lai, H. W. H. et al. Hydrocarbon ladder polymers with ultrahigh permselectivity for membrane gas separations. *Science* **375**, 1390–1392 (2022).
13. Sanaeepur, H. et al. Polyimides in membrane gas separation: monomer's molecular design and structural engineering. *Prog. Polym. Sci.* **91**, 80–125 (2019).
14. Filippidi, E. et al. Toughening elastomers using mussel-inspired iron-catechol complexes. *Science* **358**, 502–505 (2017).
15. Wang, S. et al. Facile mechanochemical cycloreversion of polymer cross-linkers enhances tear resistance. *Science* **380**, 1248–1252 (2023).
16. Zhang, Z. et al. Surpassing the stiffness-extensibility trade-off of elastomers via mastering the hydrogen-bonding clusters. *Matter* **5**, 237–252 (2022).
17. Li, C. et al. A highly stretchable autonomous self-healing elastomer. *Nat. Chem.* **8**, 618–624 (2016).
18. Nie, F. et al. Ru(II) catalyst enables dynamic dual-cross-linked elastomers with near-infrared self-healing toward flexible electronics. *Adv. Funct. Mater.* **32**, 2110616 (2022).
19. Ducrot, E. & Creton, C. Characterizing large strain elasticity of brittle elastomeric networks by embedding them in a soft extensible matrix. *Adv. Funct. Mater.* **26**, 2482–2492 (2016).
20. Fang, R., Liu, M. & Jiang, L. Progress of binary cooperative complementary interfacial nanomaterials. *Nano Today* **24**, 48–80 (2019).
21. Fang, R. et al. Bioinspired interfacial materials: from binary cooperative complementary interfaces to superwettability systems. *Adv. Mater. Interfaces* **5**, 1701176 (2018).
22. Wang, B. & Wang, T. Binary cooperative complementary membranes: a perspective. *Adv. Mater. Interfaces* **9**, 2200592 (2022).
23. Yan, C. & Wang, T. A new view for nanoparticle assemblies: from crystalline to binary cooperative complementarity. *Chem. Soc. Rev.* **46**, 1483–1509 (2017).
24. Wang, B. et al. Binary-cooperative ultrathin porous membrane for gas separation. *Adv. Mater.* **36**, 2309572 (2024).
25. Wang, S. et al. Advances in high permeability polymer-based membrane materials for CO_2 separations. *Energ. Environ. Sci.* **9**, 1863–1890 (2016).
26. Tong, Z. & Ho, W. S. W. Facilitated transport membranes for CO_2 separation and capture. *Sep. Sci. Technol.* **52**, 156–167 (2017).
27. Wang, B. et al. Unobstructed ultrathin gas transport channels in composite membranes by interfacial self-assembly. *Adv. Mater.* **32**, 1907701 (2020).
28. Henis, J. M. S. & Tripodi, M. K. Composite hollow fiber membranes for gas separation: the resistance model approach. *J. Membr. Sci.* **8**, 233–246 (1981).
29. Park, J. et al. Gas transport properties of PDMS-coated reverse osmosis membranes. *J. Membr. Sci.* **604**, 118090 (2020).
30. Xu, J. et al. Parametric analysis and potential prediction of membrane processes for hydrogen production and pre-combustion CO_2 capture. *Chem. Eng. Sci.* **135**, 202–216 (2015).
31. Xu, J. et al. Post-combustion CO_2 capture with membrane process: Practical membrane performance and appropriate pressure. *J. Membr. Sci.* **581**, 195–213 (2019).

Acknowledgements

T.W. acknowledges the National Key Research and Development Program of China Grant (2023YFB3210100) and the National Natural Science Foundation of China (21925405). B.W. acknowledges the National Natural Science Foundation of China (22408277) and Natural Science Foundation of Tianjin (25JCYBJC00570).

Author contributions

B.W. and C.Z. fabricated the membrane, and J.Z. conducted the characterization. X.S., H.Y. and Q.L. conducted simulation analysis. J.Y. and J.L. tested the membrane separation performance. B.W. and T.W. coordinated the writing of this paper. All authors discussed the results and commented on the manuscript.

Competing interests

The authors declare no competing interests.

Additional information

Supplementary information The online version contains supplementary material available at https://doi.org/10.1038/s41467-026-69949-1.

Correspondence and requests for materials should be addressed to Bo Wang or Tie Wang.

Peer review information *Nature Communications* thanks the anonymous reviewers for their contribution to the peer review of this work. A peer review file is available.

Reprints and permissions information is available at http://www.nature.com/reprints

Publisher's note Springer Nature remains neutral with regard to jurisdictional claims in published maps and institutional affiliations.

Open Access This article is licensed under a Creative Commons Attribution-NonCommercial-NoDerivatives 4.0 International License, which permits any non-commercial use, sharing, distribution and reproduction in any medium or format, as long as you give appropriate credit to the original author(s) and the source, provide a link to the Creative Commons licence, and indicate if you modified the licensed material. You do not have permission under this licence to share adapted material derived from this article or parts of it. The images or other third party material in this article are included in the article's Creative Commons licence, unless indicated otherwise in a credit line to the material. If material is not included in the article's Creative Commons licence and your intended use is not permitted by statutory regulation or exceeds the permitted use, you will need to obtain permission directly from the copyright holder. To view a copy of this licence, visit http://creativecommons.org/licenses/by-nc-nd/4.0/.

© The Author(s) 2026